ASCEND
November 15-17, 2021, Las Vegas, Nevada & Virtual
ASCEND 2021

10.2514/6.2021-4102

Check for updates

The AEROS Mission: Multi-Spectral Ocean Science Measurement Network via Small Satellite Connectivity

Cadence Payne*, Miles Lifson, Albert Thieu, Hannah Tomio, Peng Mun Siew, Christian Haughwout, Dava Newman†, Kerri Cahoy‡
Massachusetts Institute of Technology, Cambridge, MA, 02139

André Santos and Tiago Hormigo
Spin.Works, R. de Fundões 121 n° 15, 3700-121 São João da Madeira, Portugal

Manuel Coutinho and Helder Silva
Edisoft, S.A, R. Calvet de Magalhães 245, Paço de Arcos, Portugal

Downloaded by MIT Libraries on October 26, 2026 | http://arc.aiaa.org | DOI: 10.2514/6.2021-4102

Earth's oceans are an integral sub-system of our planet and an invaluable resource. Consequences of climate change threaten to have substantial and irreversible negative effects on our oceans, making it crucial to quickly understand and quantify climate impact due to increased human activity. Near-continuous, large-scale monitoring from space is revolutionizing the way we study and monitor the ocean, and Nanosatellites can provide affordable platforms to facilitate and expedite this process with increased spatial, spectral, and temporal resolution and coverage. AEROS is a 3U CubeSat developed for operation in Low-Earth Orbit (LEO, 450 km) that will demonstrate improved spectral coverage using a narrowband (10 nm), multi-spectral (150+ measurement bands) optical spectrometer imaging payload to sense ocean color. This work presents results from a radiometric model developed to assess the imager's ability to perform ocean color observations. We show that with the imager's current configuration positioned in our selected orbit, we can achieve more than 10 dB signal-to-noise ratio margin for each of the mission's target observation bands. We present methods for developing the radiometric tool, creation and use of custom atmospheric models using MODTRAN, and the mission's orbital selection process.

I. Nomenclature

$3U$	=	CubeSat standard specification for a spacecraft of size 10 x 10 x 30cm^3
D_{ap}	=	aperture diameter of the imaging optic
CSSI	=	Center for Space Standards and Innovation
f	=	focal length
f/#	=	f-number, a ratio of focal length to the entrance pupil diameter
FOV	=	field-of-View
ISS	=	International Space Station
NIR	=	near-infrared (780 nm - 2500 nm)
VNIR	=	visible and near-infrared (350 nm - 1000 nm)
λ	=	wavelength, expressed in units of nanometers in this work
SNR	=	Signal-to-Noise Ratio
N_{well}	=	well depth/capacity
N_d	=	dark noise
N_q	=	quantisation noise
N_{fpn}	=	fixed-pattern noise
N_r	=	RMS readout noise
N_t	=	temporal noise

*Research Assistant, Department of Aeronautics and Astronautics, 77 Massachusetts Ave, Cambridge, MA 02139.
†Director, MIT Media Lab, 75 Amherst Street, Cambridge, MA 02139.
‡Assistant Professor, Department of Aeronautics and Astronautics, 77 Massachusetts Ave, Cambridge, MA 02139.

Copyright © 2021 by the American Institute of Aeronautics and Astronautics, Inc. All rights reserved.

L_{atm}	=	atmospheric loss
L_{opt}	=	optical path loss
QE	=	quantum efficiency
ROI	=	Region of Interest
SSO	=	Sun-Synchronous Orbit
MODTRAN	=	MODerate resolution atmospheric TRANsmission program
dB	=	decibels

II. Introduction

The Earth's oceans cover roughly 71% of the planet's surface, so it follows that these large bodies are intimately intertwined with the planet's climate and weather systems [1]. Monitoring key features of the ocean provides critical insight to how its behavior is changing within the context of our shifting climate. In-situ, airborne, and spacecraft-based observations of ocean features are often used as inputs to climate and weather models. Nanosatellites offer opportunities for rapid revisit of key ocean features with high spectral resolution (100 - 150+ measurement bands), and distributed nanosatellite constellations provide dedicated solutions that offer revisit times on the order of hours.

This paper presents a design study for use of a multi-spectral imager (10 nm bandwidth) onboard the AEROS nanosatellite to monitor ocean color. AEROS is a technology demonstration that serves as a precursor to an ocean-observing constellation. We present a design study that assesses measurement performance achieved with a multi-spectral imager targeting ocean color, orbit selection for the mission target region of interest (ROI), and coverage achieved with the sensor over the observed region. We provide a detailed overview of the mission given different orbital configurations and consider how each configuration affects our anticipated ground coverage. We discuss the creation of models and parameter selection that simulates atmospheric conditions over the mission's ROI. Lastly, we provide an overview of methods for feeding outputs from the atmospheric model into a tool that simulates the imager's sensitivity to each of our target measurement bands via a radiometric approach. Preliminary results from the simulation are discussed.

Downloaded by MIT Libraries on October 26, 2026 | http://arc.aiaa.org | DOI: 10.2514/6.2021-4102

A. Project Motivation

Our oceans contain millions of plants and animals whose existence sustains ecosystems that are critical for maintaining oxygen and food supplies. For example, marine plant species such as phytoplankton, kelp, and algal plankton produce approximately 70% of the oxygen in the Earth's atmosphere and are key for locating high volumes of larger marine life, a metric useful for local fishermen [2]. Phytoplankton play an especially critical role in regulating our planet's climate by capturing atmospheric carbon dioxide and transferring it to the ocean during photosynthetic processes [2]. Additionally, according to the United Nations, roughly 40% of the global population lives in coastal regions, meaning their well-being in these areas is directly correlated to the behavior of the oceans bordering their homes [3]. These combined contributions to our planet's overall well-being make our oceans essential for technological, scientific, economic, and social development. Climate change threatens severe damage to our oceans, making it critical to quickly understand and quantify behavioral changes on large scales to rapidly inform climate mitigation techniques.

Ocean color observations are often used as proxies for monitoring critical features like ocean fronts, current patterns, phytoplankton concentrations, and locations of anthropomorphic input such as coastal runoff and oil spills [4]. Multi-spectral imaging of ocean color proves an invaluable resource for monitoring its current and evolving behavior. Deployment of in-situ instruments such as buoys and gliders is expensive and requires physical setup and monitoring with humans-in-the-loop. Though these devices can achieve high temporal resolution, they are limited in spatial coverage, requiring large, distributed networks of instruments to fully sense target regions. Nanosatellites are potential solutions for missions that are willing to accept higher risk and resource-constrained conditions to access space-based platforms rapidly and at lower costs compared with larger, more traditional spacecraft and in-situ instruments. Nanosatellite platforms offer a solution for keeping pace with the rapidly changing climate via large-scale deployment of space-based, ocean-sensing instruments that can provide near-continuous measurements of ocean features.

B. Ocean Observing Instruments

Since the launch of NASA's SeaSat in 1978, satellite-based remote sensing has revolutionized the scientific study of Earth's oceans. From their vantage point on orbit, these spacecraft have a global perspective of the complex and dynamic environment of our planet. Surface-based sensors are typically constrained either spatially (in the case of networks of buoys that are limited to specific regions) or temporally (in the case of ship or glider-based sampling campaigns). In

contrast, satellites can offer broader coverage and higher temporal resolution measurements. With mission lifetimes spanning years, even decades, satellite-based instruments have facilitated the creation of continuous data records that have been critical to understanding long term shifts in ocean and atmospheric processes. While SeaSat's mission was unexpectedly cut short, it nonetheless demonstrated key instruments for ocean observation and paved the way for modern missions. SeaSat's instruments, which included a radar altimeter, synthetic aperture radar (SAR), scatterometer, visible and infrared radiometer (VIRR), and microwave radiometer, exemplify the breadth of satellite sensors and techniques used for ocean observation and the numerous attributes that can be measured from orbit [5].

By far the broadest category of ocean-observing instruments, radiometers and spectrometers are passive remote sensors that measure electromagnetic (EM) radiation. Radiometers in particular can be designed to operate in the ultraviolet (UV) through microwave wavelengths. These instruments are used to detect the intensity of radiation emitted from a target object (in the thermal infrared or microwave regions), reflected off the object from an outside source (typically the Sun, in the visible and near-infrared regions), or some combination thereof. Spectrometers (or spectroradiometers) also measure incident EM radiation, focusing on the spectral components of the radiation by distinguishing different wavelengths and measuring their relative intensities as a function of wavelength. Imaging instruments represent these measurements as 2D images and are referred to as multispectral imagers or hyperspectral imagers based on their spectral range and resolution [6][7]. For ocean observation, these instruments can be used to measure ocean color in the visible and near-infrared regime and sea surface temperature in the thermal infrared regime [8].

Currently, imaging instruments such as the Moderate Resolution Imaging Spectroradiometer (MODIS) on NASA's Terra and Aqua satellites, the Visible and Infrared Imager/Radiometer Suite (VIIRS) on the Suomi National Polar-orbiting Partnership (Suomi-NPP) and Joint Polar Satellite System-1 (JPSS-1) satellites, and the Ocean and Land Colour Instrument (OLCI) on ESA's Sentinel-3A and Sentinel-3B provide continuous monitoring of the Earth. The MODIS instruments feature 36 discrete bands, with center wavelengths ranging from 412 nm to 14.24 um and bandwidths from 10 nm to 0.5 um. The spatial resolution varies by band, ranging from 250 m to 1 km, and each instrument has a swath width of 2330 km, providing global coverage every 1-2 days [9][10]. VIIRS is the successor to MODIS, and features 22 spectral bands, with center wavelengths ranging from 415 nm to 12.013 um and bandwidths from 20 nm to 1 um. It has two spatial resolutions, 375 m and 750 m, with a swath width of 3000 km to provide near global coverage every day [11]. OLCI has 21 bands, ranging from 400 nm to 1020 nm with bandwidths from 2.5 nm to 40 nm. The instrument has a full spatial resolution is 300 m and a swath width of 1270 km, providing global coverage every 4 days [12]. These major missions represent significant endeavors: the payload instruments were large, complex, and costly to develop, designed to operate for several years and carried to orbit by substantial spacecraft platforms. While these instruments have been essential to advancing the scientific study of land, oceans, and atmospheres, their broad scope may not be appropriate for highly targeted applications necessitating a specific spectral band, spatial resolution, or high revisit rate coverage of specific regions of interest.

C. CubeSat Justification

Sensors on space-based platforms offer solutions for effectively and frequently monitoring large swaths of the ocean, and are therefore indispensable tools for monitoring climate related phenomena. The CubeSat (nanosatellite) platform offers a low-cost (typically <$10 million for construction and launch) approach for quickly (typically 3-4 year development times) performing novel technology demonstrations, albeit with limitations in size, weight, and power (SWaP). Compared with airborne imagers such as NASA's Airborne Visible/Infrared Imaging Spectrometer (AVIRIS), an airborne hyperspectral imager that supports 224 contiguous detection bands from 380 nm to 2500 nm each with 10 nm resolution, CubeSats also suffer from reduction in measurement quality and data quantity due to on-board resource limitations [13]. Nonetheless, CubeSats offer high-spectral resolution, high-temporal resolution, and high-coverage solutions for autonomously performing ocean measurements on large scales.

CubeSats provide gap filling solutions via intentional selection of measurement bands. They fill gaps in spectral observations by hosting sensors designed to measure bands between coverage provided by dedicated ocean observing instruments such as MODIS and VIIRS, and complement existing measurements by capturing identical spectra with increased temporal resolution. As climate scientists work to understand and identify high-impact regions that are meaningful to monitor, CubeSats can be developed quickly to monitor these areas of interest. CubeSat constellations observe large areas of the planet and could aid in quickly monitoring high-priority regions with increased diversity in regional coverage. Additionally, constellations provide potential improvements to communication frequency with networks such as ARGOS, a distributed network of fixed and mobile (biologged) instruments used to collect and

Downloaded by MIT Libraries on October 26, 2026 | http://arc.aiaa.org | DOI: 10.2514/6.2021-4102

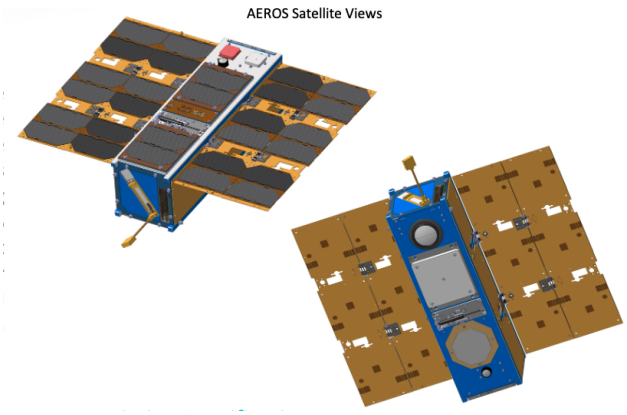


Fig. 1 CAD Renderings of the AEROS CubeSat courtesy of CEiiA

Downloaded by MIT Libraries on October 26, 2026 | http://arc.aiaa.org | DOI: 10.2514/6.2021-4102

distribute environmental data to spacecraft receivers [14]. Large, distributed networks of platforms with ARGOS receivers can decrease time between spacecraft contact with network transmitters, increasing non-proprietary access to ARGOS data. Lastly, the CubeSat platform is unique in that it is easily customizable for diverse sensor suite types. These platforms, while resource-limited, push technical bounds in forcing the miniaturization of traditional sensor packages while challenging developers to maintain sensor sensitivity and data integrity.

III. The AEROS Mission

The AEROS nanosatellite (see Figure 1 is a 3U (10 x 10 x 30 cm^3), 5 kg CubeSat designed to operate in Low-Earth Orbit (LEO) at a 450 km altitude. AEROS hosts a miniaturized multi-spectral imaging payload for monitoring and forecasting ocean behavior. The science-based measurement objectives involve sensing ocean color, front locations, and fauna concentrations using over 150 VNIR/NIR measurement bands, each with 10 nm bandwidth. In addition to its imaging payload, AEROS hosts a custom Software Defined Radio (SDR) configured based on a Zynq-7000 SoC with use of the GNU Radio software. The SDR is intended to support connectivity with ground stations, autonomous vehicles, buoy-mounted receivers and biologgers secured to sea life. Table 1 provides an overview of key mission specifications. Table 2 in the "Multi-spectral Imaging Payload" section provides key specifications on the payload configuration.

Table 1 Optics and Detector Parameters of the Spin.Works Multi-Spectral Imager

Specification	Value
CubeSat Specification	3U (10 x 10 x 30 cm^3)
Mass	< 5 kg
Orbit Altitude	LEO: 450 km
Orbital Period	90 minutes
Payload Type	Miniaturized Multi-Spectral Imager, Software-Defined Radio
Ground Sampling Distance (GSD)	49.5 m at 450 km [15]
Region of Interest	Portuguese Coast

A. Mission and Science Objectives

The AEROS mission has three primary, high-level mission objectives:

- Monitor and value the ocean via a suite of nanosatellite payloads
- Develop a nanosatellite as precursor to a future ocean sensing constellation
- Advance technical know-how of Portuguese research entities

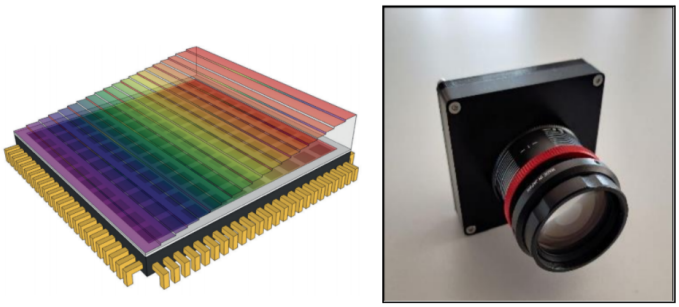


Fig. 2 Multi-spectral imaging payload: LineScan sensor (left) and Spin.Works camera lens assembly (right) [15]

Downloaded by MIT Libraries on October 26, 2026 | http://arc.aiaa.org | DOI: 10.2514/6.2021-4102

The mission's primary science objective involves measuring ocean color to determine oceanfront and fauna locations. There exists a need for increased spatial resolution (# of pixels), spectral coverage (# of measurement bands), and temporal resolution (revisit rates) to advance collective climate change assessment and mitigation techniques. AEROS intends to target this need by offering high-spectral coverage via its multiband optical spectrometer payload. The mission is a technology demonstration that will space-qualify its custom built multispectral imager and characterize its use for observation of coastal regions. AEROS will target regions along the Portuguese coast and will focus on characterizing the imager's performance for ocean color measurements. These miniaturized multi-spectral payloads are tunable (in terms of band selection) to support a diverse set of measurement types for future missions. The goal for an eventual constellation of AEROS-like nanosatellites will drastically reduce revisit rates over key regions of interest down to the order of hours, compared to days for a single spacecraft, providing necessary improvements to temporal resolution.

AEROS is developed and supported by the MIT Portugal program, a resource that combines efforts from MIT, namely the Department of Aeronautics and Astronautics for this work, with private Portuguese companies and universities. This mission is unique in that successful launch and operation will both support Portugal's effort in acquiring a new status in space, as well as boost Portuguese technological ability and competency for performing ocean observations. Lastly, this work is aligned with the United Nations' Sustainable Development Goals by providing opportunities to collect data for better informing climate action and monitoring the state of ocean life [16].

B. The Multi-Spectral Imaging Payload

AEROS will host a custom, miniaturized multi-spectral camera assembly from Spin.Works that combines a 50 mm, f/2.8 lens (FOV of 12.8°, full angle) with an IMEC LS150, a Commercial Off-the-Shelf (COTS) multi-spectral linescan image sensor (see Figure 2) [15][17]. The IMEC LS150 is a CMOS detector with multi-spectral filters integrated on top of the sensor's aperture to effectively disperse incident light over 100+ (VNIR) to 150+ (NIR) contiguous measurement bands [15][17]. The hyperspectral camera can support measurement wavelengths from 470 - 1000 nm each with < 10 nm bandwidth (FWHM) and has an image resolution of 2048 x 1088 pixels [15][17]. The sensor is configurable to allow users to tune band sensitivity to the desired measurement range, and can support up to 2720 scanned lines per second with 7 dedicated lines for each band [17]. The combined assembly volume is less than 1U (50 x 64 x 101 mm^3) and is light-weight (300 g) [15]. Table 2 provides an overview of relevant parameters for the imager assembly.

IV. Orbit Selection

An orbit study was conducted to assess several factors including orbital lifetime, ground station access, power generation, and sensor coverage/revisit rates over the ROI to inform launcher selection. A variety of ride-share launch options were considered, as seen in Table 3, including several sun-synchronous orbit (SSO) launchers, Cygnus deployment, and deployment from the International Space Station (ISS). The team is currently targeting an ISS deployment with greater schedule flexibility afforded due to the frequent ISS launch cadence. Analysis showed than any 500 km or lower launch listed in Table 3 would likely be adequate to meet the mission's power, coverage, communications, and orbital debris mitigation lifetime requirements [18].

Table 2 Optics and Detector Parameters of the Spin.Works Hyperspectral Imager [15][17]

Parameter	Value
HSI Package Mass	300 g
HSI Package Volume	50 x 64 x 101 mm^3
Optics Aperture Diameter (D_{ap})	18 mm (front-end lens)
Focal Length (f)	50 mm
f/#	2.8
Pixel Pitch	5.5μm
Max Shutter Speed	6.5 ms (at 450 km)
FOV	12.8° (full angle, horizontal), 6° (vertical), 14.6° (diagonal)
Spectral Bandpass (λ_{min} - λ_{max})	470 nm - 1000 nm
Spectral Bandwidth (λ_0 - λ_f)	10 nm (collimated)
Sensor Resolution	2048 x 1088
Line Rate	2720 lines/sec
Line Allocation	7 sensor lines/band
Dynamic Range	60 dB
Well Depth (N_{well})	13.5 ke^-
Dark Noise	125 e/s @ 25°C
Quantum Efficiency	4% - 24% (10% avg.)

Table 3 Launch options considered

	ISS	Cygnus	Soyuz	Falcon 9	Vega/Vega-C	Firefly Alpha	Epsilon/H3
Launch Site	N/A	Wallops	Vostochny/Baikonur	Vandenberg	CSG Kourou	Vandenberg	Uchinoura
Launch Period	Dec 2022 (assumed)	Mar 2023 (assumed)	Dec 2022 (Q4 2022)	Dec 2022 (from Q4 2022)	Mar 2023 (Q1 2023)	Dec 2022 (from Q4 2022)	Oct 2022
Altitude	420 km	465/500 km	530 km SS0	500 km SSO	500 km SSO	500 km SSO	560 km SS0
Type	51.6 deg	51 deg	SSO 10:30 LTAN	SSO 9:00 LTDN	SSO 10:30 LTDN	SSO 10:30 LTAN	SSO 9:30 LTAN

Two potential spacecraft configurations were originally considered, as seen in Figure 3, with significant implications for drag and power generation. The minimum drag configuration was selected by the design team because it allowed for significantly better internal configuration of spacecraft components and a greater nadir-pointing surface for instruments and antennas.

.

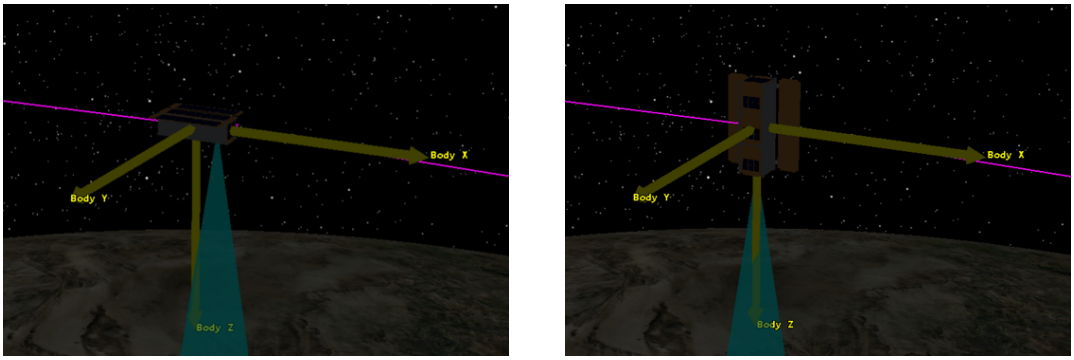
A. Orbital Lifetime/Attitude

The spacecraft is assumed to weigh 5.5 kg with attitude defined according to a three-tier priority list:

1) If over the ROI, the spacecraft will point nadir to take observations;
2) Else if the spacecraft is illuminated, the spacecraft will align to the Sun vector with a nadir constraint;
3) Else the spacecraft will align itself with its velocity vector using a nadir constraint for the purpose of drag-minimization.

Initial lifetime estimates were computed for cross-sectional areas of 100 cm^2, 300 cm^2, 600 cm^2, 900 cm^2, and 1500 cm^2 using a Jacchia-Roberts atmospheric model and predicted solar flux levels provided by the Center for Space Standards and Innovation (CSSI) under nominal conditions and at -3, -2, -1, +1, +2, and +3 standard deviations. These

Downloaded by MIT Libraries on October 26, 2026 | http://arc.aiaa.org | DOI: 10.2514/6.2021-4102



(a) Minimum Drag Configuration (sensor on the 3U side of spacecraft)

(b) Pointing Instrument Nadir Configuration (sensor on 1U side of spacecraft)

Fig. 3 The two considered sensor configurations. The minimum drag configuration was chosen due to greater nadir-pointing surface and better internal geometry.

Downloaded by MIT Libraries on October 26, 2026 | http://arc.aiaa.org | DOI: 10.2514/6.2021-4102

cross-sectional areas correspond to the range of possible values achievable with different attitude configurations.

Out of an abundance of caution, candidate orbits were selected such that the spacecraft would be unlikely to significantly exceed 25 years of post-mission orbital lifetime even if it failed on deployment, assumed a drag-minimizing attitude, and experienced atmospheric density associated with solar flux levels below predictions. This is a very conservative standard intended to ensure compliance with internationally recognized norms for responsible behavior. These criteria rule out deployment to an altitude above 500 km and eliminated the Soyuz and Epsilon/H3 launch options from consideration.

Using the set of attitude priority rules at the start of this section, the average cross-sectional area of the 3U spacecraft with deployed panels is approximately 6U for both ISS-deployment (603 cm^2) and a 500 km Cygnus deployment (601 cm^2), meaning the spacecraft will re-enter significantly sooner than the drag-minimized case.

As seen in Figure 4, an ISS deployment offers at least six months of orbital lifetime under any anticipated solar flux conditions and orbital lifetime short enough to satisfy orbital debris mitigation concerns even if the spacecraft fails on deployment and cannot control attitude. The Cygnus 465 km deployment offers longer orbital lifetime of 1-3 years as seen in Figure 5, but still will not likely exceed 25 years on-orbit in the event of a failure. Under a worst-case scenario, a 500 km Cygnus deployment may exceed the 25 year rule by approximately 1.3 years under nominal solar conditions and almost 15 years under solar flux conditions three standard deviations below the nominal prediction. It would provide a nominal mission lifetime of approximately 2-5 years (see Figure 6).

At low altitudes, higher atmospheric drag can impair spacecraft attitude control and impact imaging and communications operations. Accordingly, functional mission lifetime may be shorter than absolute orbital lifetime. In recognition of this fact, orbital lifetime above 300 km was calculated for each of these orbits, corresponding to likely mission operational lifetime and is seen in Figure 7 for nominal solar flux conditions. This cut-off shortens mission lifetime by approximately 30-60 days as compared to orbital lifetime.

B. Power

As seen in Figure 8, the spacecraft was modeled as featuring 28 solar cells, each with an area of 26.62 cm^2, all aligned to the -Z direction (zenith). Panels were assumed to be 30% efficient (based on values for the selected panels at `https://gomspace.com/shop/subsystems/power/nanopower-dsp.aspx`), with 10% internal losses [19, 549] for an effective efficiency of 27%.

Spacecraft power generation was modeled using both STK's solar panel tool and an internal MATLAB tool (developed within MIT STARLab by Riley Fitzgerald), which were compared and showed similar mean power generation (within a few Watts) and power curve shapes. As seen in Figure 9, the SSO orbit offers more consistent power generation over the course of the year (simulated from December 2022 until December 2023). All the ISS and Cygnus orbits perform similarly.

For ISS deployment, median power generation under tumbling conditions was calculated to be 5.59 Watts, corresponding to median power generation of 8.55 Watt hours per orbit.

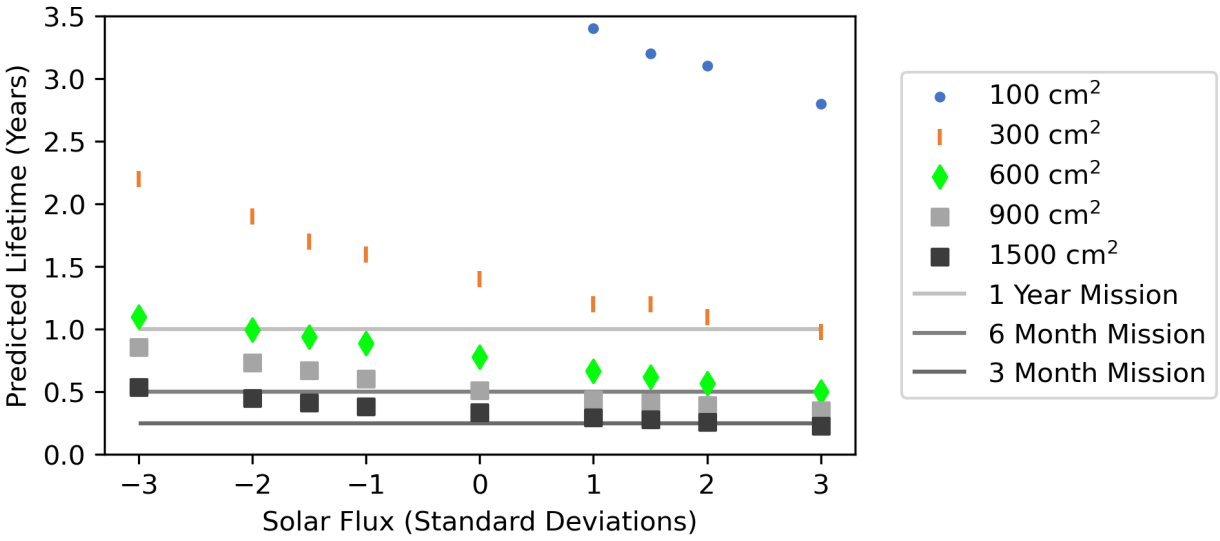


Fig. 4 ISS Deployment Orbital Lifetime. An orbital lifetime of 6-12 months is likely for the anticipated 600 cm^2 average cross-sectional area.

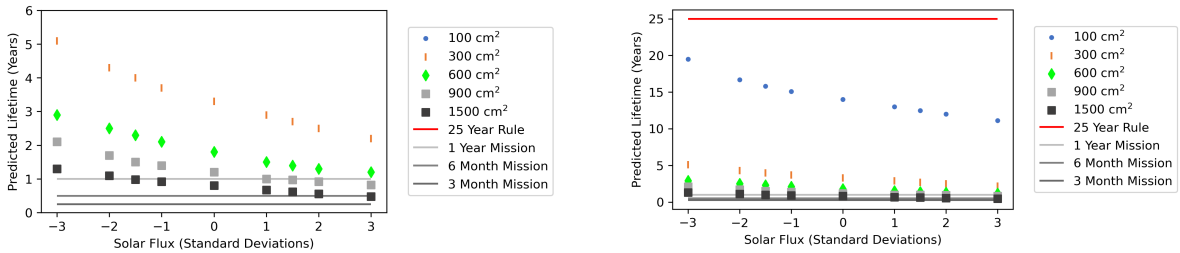


Fig. 5 Cygnus 465 km Deployment. Nominal mission lifetime is 1-3 years, with 25 year rule compliance under all conceivable conditions.

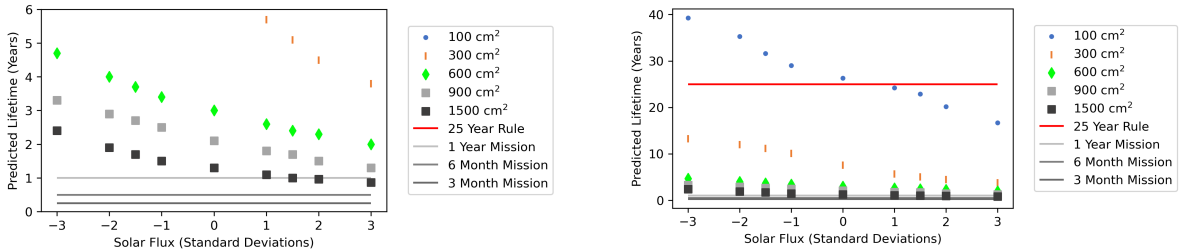


Fig. 6 Cygnus 500 km Deployment. Nominal mission lifetime is 2-5 years, with potential 25 year rule violation for nominal and sub-nominal solar flux levels.

Downloaded by MIT Libraries on October 26, 2026 | http://arc.aiaa.org | DOI: 10.2514/6.2021-4102

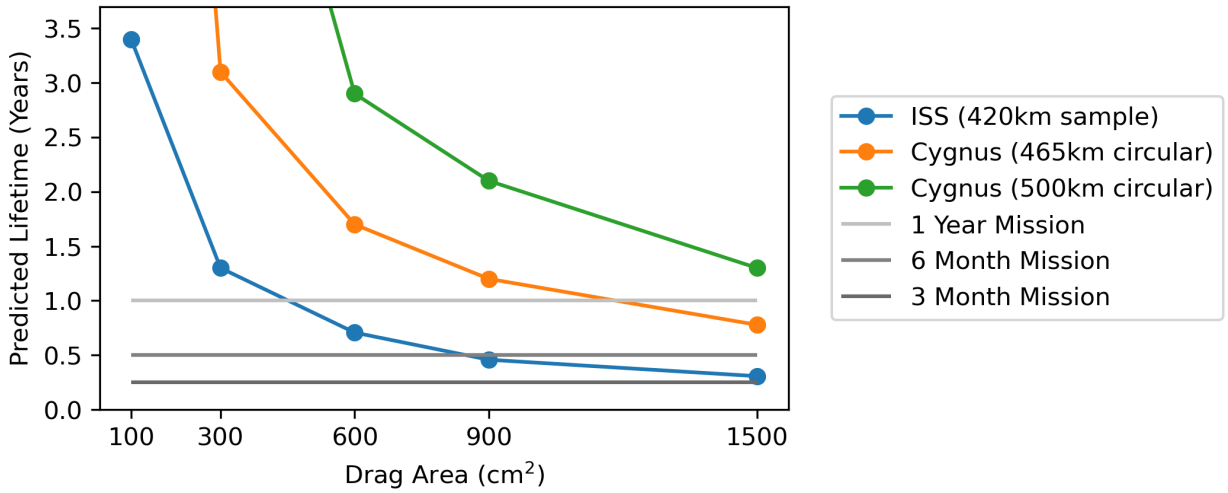


Fig. 7 Operational Lifetimes (300 km cut-off altitude, nominal solar flux). The three analyzed orbits provide at least six months of mission lifetime under nominal conditions.

V. Coverage

The target ROI is the ocean near the Portuguese shore, specifically the Portuguese Extended Continental Shelf and Portuguese Exclusive Economic Zones (Mainland, Azores, and Madiera). The two potential ground stations are located at Matosinhos (41.172° N, -8.679° W) and Santa Maria Station (37.000° N, -25.135° W), with both assumed to have an overly optimistic 0° minimum elevation angle requirement.

The hyperspectral imager sensor field of view was modeled as a 12.8° by 6.0° full angle rectangle with the long axis aligned to the +Y axis of the spacecraft. As seen in Figure 11, the higher altitude of the 500 km Cygnus deployment significantly reduces mean revisit time versus ISS deployment or the 465 km Cygnus deployment due to wider swath width. For comparability purposes, the orbits in this figure were all simulated for an 180 day period beginning on June 1, 2023, roughly corresponding to the anticipated ISS-deployment orbital lifetime under nominal conditions. The 465 and 500 km Cygnus deployments will remain in orbit longer than this time period, and coverage will shift as the spacecraft decays. Because these orbits are not sun-synchronous, there is viability in the proportion of passes that occur during sunlight over the mission lifetime's.

VI. Radiometric Approach

Radiometry is defined as the measurement of light across a portion of the electromagnetic spectrum and is directly measured by remote sensing instruments [20]. Radiometric measurements are described in terms of absolute units of photons*sr^{-1}* s^{-1}, and radiation intensity is described in terms of radiance or irradiance, terms that are often mistakenly used interchangeably [21] [22][23]. For ocean color measurements, we target observation of top-of-the-atmosphere (TOA) spectral radiance in units of W*m^{-2}*sr^{-1}*μm^{-1}.

Radiometric analysis is often performed for spacecraft instrumentation designed to remotely sense some target source. For this work, we assume a remote sensing payload composed of a camera lens assembly, a passive hyperspectral grating filter, and a digital CMOS detector. Our system acquires images in the visible to near-infrared range (350 nm - 1000 nm), though most target bands in this work are in VIS (350 nm - 750 nm), and our signal source is TOA spectral radiance of the ocean along or near the Portuguese coast.

A. Target Measurement

Ocean color serves as a proxy for monitoring several phenomena including ocean fronts, eddies, and fauna concentrations. It is also possible to extract measurements of Color Dissolved Organic Matter (CDOM) and other suspended particles from ocean color observations [24][25][26]. Additionally, bio-optical measurements of both ocean color and CDOM are useful proxies for estimating Sea Surface Salinity (SSS) [27]. Lastly, it is necessary to monitor bands useful for atmospheric correction (e.g. VIIRS 746 nm band calibrated for aerosol and optical depth retrieval,

Downloaded by MIT Libraries on October 26, 2026 | http://arc.aiaa.org | DOI: 10.2514/6.2021-4102

Downloaded by MIT Libraries on October 26, 2026 | http://arc.aiaa.org | DOI: 10.2514/6.2021-4102

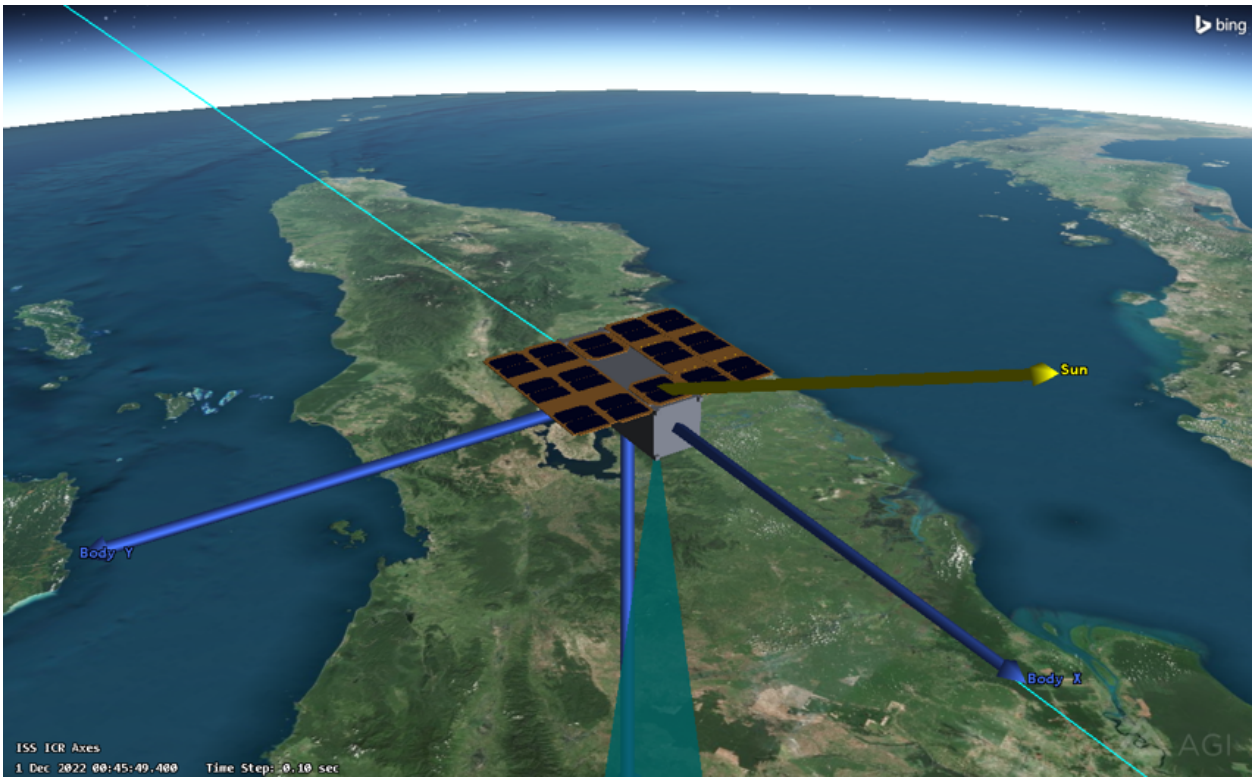


Fig. 8 The modeled solar cell configuration. All cells face the -Z direction.

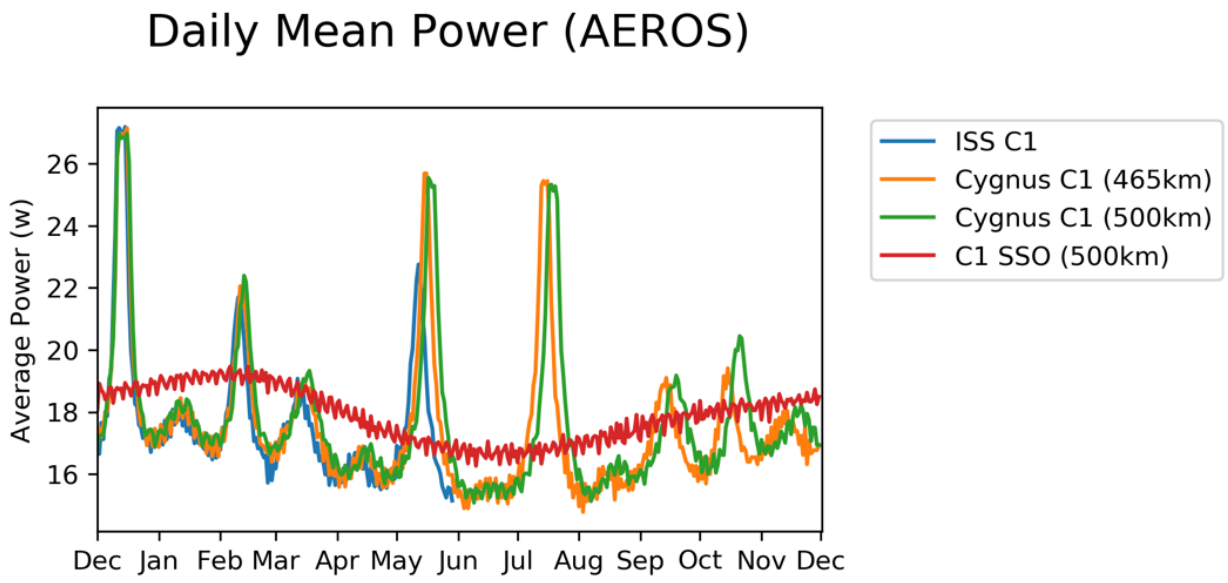


Fig. 9 The SSO orbit offers less variable mean daily power generation over the course of the year.

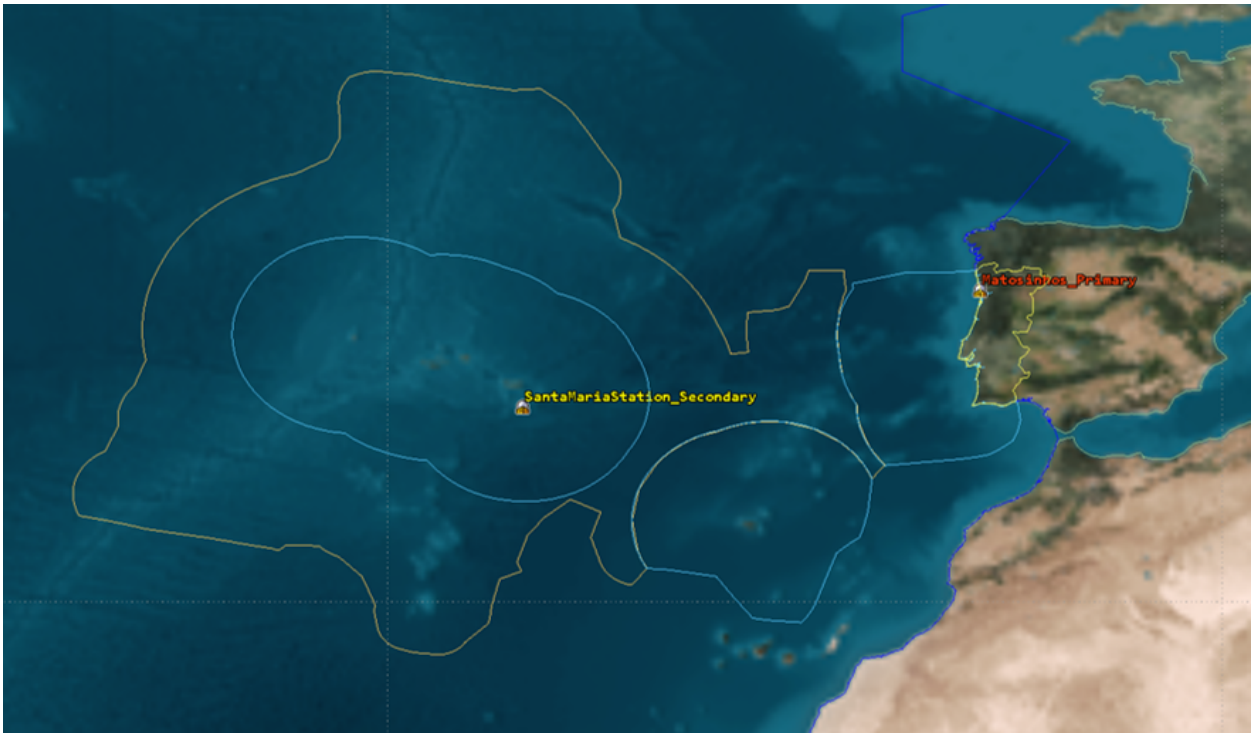


Fig. 10 The ROI is composed of the Portuguese Extended Continental Shelf and the Portuguese Exclusive Economic Zones associated with Mainland Portugal, the Azones, and Madiera.

though details of this process fall outside the scope of this work [28]. We have identified a subset of measurement bands that are typically prioritized for observing ocean color. Table 4 shows each of AEROS' selected target bands and their respective proxies.

We observe ocean color by imaging reflected and backscattered light off the ocean's surface across multiple wavelengths [26]. For this work, we use an atmospheric modeling tool called MODTRAN to compute total top-of-the-atmosphere (TOA) spectral radiance at our detector for each band. The total radiance output from MODTRAN is expressed in units of W$*cm^{-2}*sr^{-1}$ / cm^{-1} in terms of spectral radiance per wave number. Our radiometric tool converts this value to total spectral radiance in units of W$*m^{-2}*sr^{-1}*\mu^{-1}$ for each wavelength, the aforementioned form. This value accounts for light from the Sun reflected off the ocean surface, as well as light scattered into the sensor's observation path from other sources and atmospheric effects. The resulting total TOA spectral radiance values serve as the source input to the radiometric model. To simulate coastal imaging, we have configured the MODTRAN model to consider conditions over Lisbon, Portugal's capital and a coastal city.

B. Radiometric Methodology

Our radiometric analysis assumes the form of a detailed mathematical model that captures properties of the observed signal radiance, path geometry, atmospheric effects, and effects from noise/loss inherent to the detector. Figure 12 provides a detailed overview of our method, including all parameters considered for computing the signal-to-noise ratio (SNR) at each wavelength center in the sensor's spectral bandpass. SNR is often referenced to describe image quality given the ratio of the observed signal strength to the noise and loss experienced along the observation path [29]. We use the described technique to simulate our sensor's SNR for imaging ocean color along the Portuguese coast.

Radiance (L_{typ}) from our target is provided by the output of the MODTRAN model. We average the simulated radiance values over the imager's 10 nm bandwidth and use this value as our input parameter. It should be noted that MODTRAN radiances account for atmospheric loss and scattering effects along the imager's simulated path. We consider an additional term for path loss concerning the optical-front end's transmissivity, and we calculate our source irradiance (E) as:

Downloaded by MIT Libraries on October 26, 2026 | http://arc.aiaa.org | DOI: 10.2514/6.2021-4102

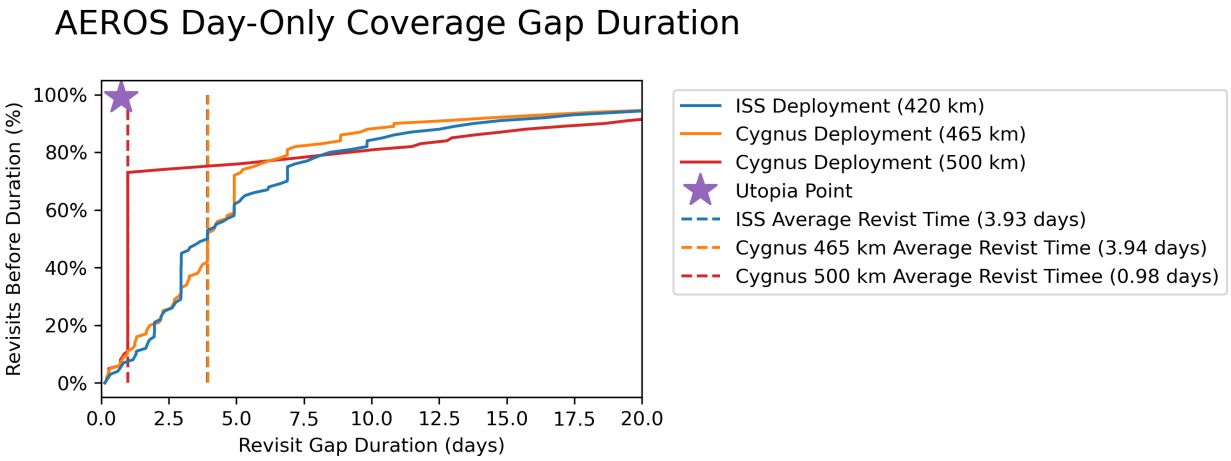


Fig. 11 The ISS and 465km Cygnus Orbits have

Table 4 Target Measurement Bands and Associated Ocean Proxy

Wavelength Center (nm)	Proxy
470	Ocean Color
488	SSS
490	Ocean Color
540	Ocean Color, SSS
555	Ocean Color, SSS
625	Ocean Color, SSS
650	CDOM
680	SSS
746	Atmospheric Correction
865	Ocean Color, SSS

$$E = \int_{\lambda_0}^{\lambda_f} L_{typ} * (1 - Loss_{opt})\, d\lambda \quad [W * m^{-2} * sr^{-1}] \tag{1}$$

Where λ_0 and λ_f are the initial and final wavelengths spanning the sensor's spectral bandwidth (+/- 5 nm with target band at center) in units of microns, L_{typ} is the source spectral radiance in units of W*m^{-2}*μm^{-1}*sr^{-1}), and $Loss_{opt}$ is a decimal value representing the % transmissivity. Note that if your spectral radiance values do not consider atmospheric loss terms, an additional (1 - $Loss_{atm}$) term should be considered here.

We calculate our detector irradiance area (A_{irad}) as:

$$A_{irad} = \frac{A_{det}(A_{ap} - A_{obs})}{f^2} \quad [m^2 * sr] \tag{2}$$

Where A_{det}, A_{ap} and A_{obs} are the detector, aperture and obscuration areas in units of m^2 and f is the imager's focal length in units of meters. Obscuration areas are considered for imagers with telescope assemblies. This term is dropped for the scope of this application.

We then calculate Radiant Flux (P) to compute the total power incident at the detector from our signal:

$$P = E * A_{irad} \quad [W] \tag{3}$$

Downloaded by MIT Libraries on October 26, 2026 | http://arc.aiaa.org | DOI: 10.2514/6.2021-4102

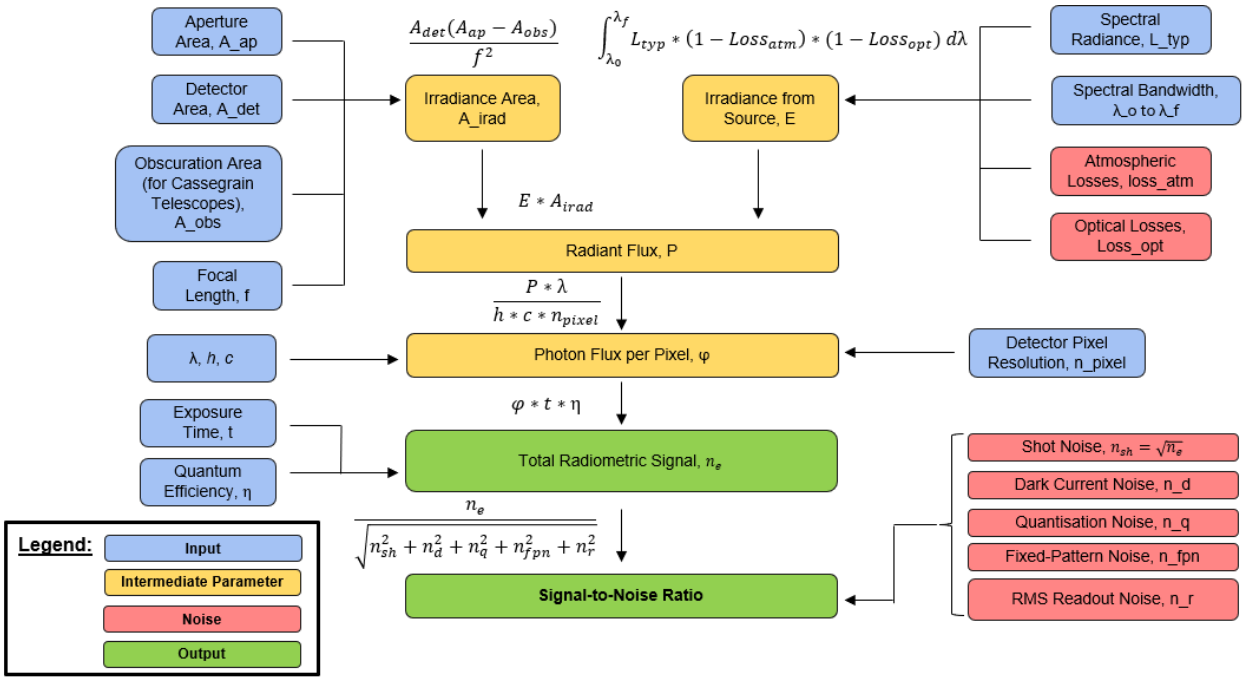


Fig. 12 Overview of the Radiometric Analysis process (credit: Albert Thieu)

This is then used to calculate the power incident on each individual pixel in the detector's array by computing the photon flux per pixel (ϕ):

$$\phi = \frac{P * \lambda}{h * c * n_{pixel}} \quad [photons/s] \tag{4}$$

Where λ is the measurement band center in units of nanometers, h is Planck's constant, c is the speed of light and n_{pixel} is the total number of pixels in the detector array. n_{pixel} computed as the product of the pixels along the x- and y-dimensions of the detector.

Next, we compute our total radiometric signal (n_e) in units of photons:

$$n_e = \phi * t * \eta \quad [photons] \tag{5}$$

Where (ϕ) is photon flux per pixel in photons/sec, t is the detector's exposure time in units of seconds, and η is the sensor's quantum efficiency.

Finally, we compute the SNR of our sensor; however, first we consider each noise term individually. Shot noise n_{sh} is simply sqrt(n_e) and is therefore spectrally dependent. This value should be calculated and handled separately for each wavelength considered.

Dark current noise (n_d) is a term resulting from charge generated internally to a detector and is present even when an imager is inactive [30] . Fixed-pattern noise (n_{fpn}) arises naturally from non-uniformity in a multi-element detector array [31]. This term is typically referred to as hot/cold pixels. RMS readout noise (nr) is the root mean square of the readout (or read) noise when all pixels are considered "active," or when the entire image plane is in use [32]. Quantisation noise (n_q) arises from uncertainty due to the analog-to-digital converter quantising the signal to digital counts [29]. This term is calculated as:

$$\sigma_{quantisation} = \frac{N_{welldepth}}{N_{DR}\sqrt{12}} \quad [e^-] \tag{6}$$

Where $N_{welldepth}$ represents the total electron capacity for each detector in the array, N_{DR} is the detector's dynamic range in terms of digital counts and sqrt(12) represents the standard deviation of a normal distribution [29].

Lastly, we compute the SNR as the ratio of total signal to the root of the sum of all of the squared noise terms:

Downloaded by MIT Libraries on October 26, 2026 | http://arc.aiaa.org | DOI: 10.2514/6.2021-4102

$$SNR = \frac{n_e}{\sqrt{n_{sh}^2 + n_d^2 + n_q^2 + n_{fpn}^2 + n_r^2}} \tag{7}$$

We present our resulting SNR values in units of dB. See Table 5 for the complete list of noise and loss parameters considered in this analysis and Table 7 for our resulting computed SNR values.

Table 5 Noise and Loss Parameters for multispectral imager[17][15]

Parameter	Value
Dark Current (N_d)	~1 e^-
Quantisation Noise (N_q)	5 e^-
Fixed-Pattern Noise (N_{fpn})	~1 e^-
RMS Readout Noise (N_r)	5 e^-
Temporal Noise (N_t)	13 e^-
Shot Noise (N_e)	λ Dependent
Atmospheric Loss (L_{atm})	Included in L_{typ}
Optical Path Loss (L_{opt})	0.9 (assuming 90% transmission)

Downloaded by MIT Libraries on October 26, 2026 | http://arc.aiaa.org | DOI: 10.2514/6.2021-4102

C. MODTRAN Model

MODTRAN is a radiation transfer (RT) model for the thermal infrared, visible and ultraviolet bands (0.2 to 10,000 um) [33]. Parameters such as atmospheric loss, sensor visibility at each band center, and optical depth are governed by regional conditions at a sensor's projected ground point. MODTRAN is a powerful tool that allows users to quickly simulate predicted, at-sensor radiance values at each wavelength with a large set of considerations for atmospheric effects along the path. Values from MODTRAN are used to calculate the total TOA spectral radiance observed at our sensor placed above the target region of interest.

Our simulations use MODTRAN's line-by-line option. This feature allows the tool to quickly generate multi-spectral radiance estimates with consideration for pressure and temperature dependencies due to molecular absorption [34]. Our model assumes a direct path from space to ground, where we define ground as sea level in Lisbon to model observation along the Portuguese coast. We consider scattering along the observed path from multiple sources including molecular scattering (most prominent in VIS bands), aerosol scattering, and effects of solar/lunar radiance scattered into the sensor's line-of-sight. We currently assume a spectral Lambertian surface given our target observation of ocean color. While some targets may be located on the boundary of ocean and land, features on land are not the target area of interest. Lambertian surfaces are typically described as isotropic or perfectly diffuse reflectors and are an appropriate proxy for representing ocean surface conditions [35]. We use the Navy Maritime aerosol model, a profile that captures the boundary layer above the ocean. It should be noted that composition of continental aerosols differs greatly from oceanic aerosols that are largely composed of sea-salt particles [36]. The Navy Maritime model considers contributions from both sea-spray aerosols and the rural aerosol continental model to represent coastal conditions.

For this work, we only vary the selection of the atmospheric model. We simulated conditions assuming both the mid-latitude summer and mid-latitude winter models to gauge how the observed total TOA spectral radiance varies seasonally. MODTRAN considers twelve ambient band model species that differ seasonally for each of the atmospheric profiles provided by the tool. Both models were run assuming that our atmospheric path was free of rain, clouds and fog at lower altitudes. Future work will assess behavior of our sensor under these conditions. The mid-latitude profile was recommended for regions at or near 45°N. We felt it was more appropriate than the tropical model (locations at or near 15°N) for Lisbon on the Portuguese coast at 38.7° N.

Preliminary results in this work only consider nadir staring (no slewing) during a pass where the spacecraft is collecting an image. Table 6 provides a more complete overview of key parameters selected for our model.

Table 6 Overview of Key MODTRAN Parameters

Parameter	Value
Atmosphere	Mid-lat, summer/winter
Atmospheric Conditions	Full visibility, no clouds/rain
Lat/Long of Region (Lisbon)	38.7°N, 9.1°W
Aerosols	Navy Aerosol Model
CO2 Mixing Ratio	360 ppmv
Surface Type	Spectral Lambertian
Observer Altitude	450 km
Inclination	51.6°
Look Angle	0° (nadir)
Time of Observation	12:00 (GMT)
Frequency Range (cm^1)	10000 - 25000 (400 - 1000 nm)

Downloaded by MIT Libraries on October 26, 2026 | http://arc.aiaa.org | DOI: 10.2514/6.2021-4102

D. Model Output

Figure 13 shows the resulting total radiance from our MODTRAN simulation for both the mid-latitude summer and mid-latitude winter atmospheric models. We have reduced the spectral range to match our sensor's spectral band pass (470 nm - 1000 nm), and our target band centers are overlaid. We plot the total radiance we anticipate seeing at our sensor located at the spacecraft's altitude over a frequency range that is slightly larger than our sensor's sensitivity. The total radiance represents the sum of path thermal radiance, surface emission, and ground reflected radiance at the observer [37]. While seasonal variations have little effect on the total radiance, it is evident that the radiance we anticipate seeing during winter months is slightly less than in summer seasonal conditions.

Work by Ientilucci 2012 as well as Pu et al., 2003 use MODTRAN to estimate at-sensor radiance for observations using NASA's AVIRIS, and both show results similar to our model's output [38][39]. Additionally, our total spectral radiance values agree closely with values reported in NASA's International Ocean-Colour Coordinating Group (IOCCG). For example, they report typical spectral radiance values at band centers of 490 nm and 555 nm as 53.1 and 33.9 $W*m^{-2}*\mu m^{-1}*sr^{-1}$ respectively, where our model shows radiances of 61.8 and 48.7 $W*m^{-2}*\mu m^{-1}*sr^{-1}$ for the mid-latitude summer case [40]. While our estimates are higher, it should be noted that we each assume different observation regions with varying assumptions for atmospheric conditions.

VII. Results

Miniaturizing a multi-spectral imaging payload is technically challenging and poses some constraints on measurement capability. For example, achieving a high number of observation bands requires imaging channels to have narrow bandwidths (10 nm), and the diameter of our optical front-end is limited in size due to the CubeSat volume limitations. Combined, these constraints reduce the number of photons collected by the detector regardless of source signal strength. We assume there are no complex pointing maneuvers that would allow our spacecraft to track the target during a pass, constraining our observations to nadir pointing. With this configuration, our imager scans the target region at the rate of the spacecraft's velocity, raising additional considerations for avoiding pixel smear. Future work is required to show overlapping areas captured in each ground scene during image collections assuming a shutter speed that avoids pixel smear.

We assume a minimum threshold of detection as 1 dB, meaning the imager collects enough photons to overcome the noise, albeit with poor image quality. Images satisfying 10:1 SNR threshold are considered to have "acceptable" image quality, while images meeting 40:1 are considered "exceptional" [41]. Our preliminary results (see Table 7 show SNRs of higher than 13 dB across each of our target bands, a comfortable value given the measurement constraints. Additionally, SNR values were calculated assuming a worst-case QE of 10% and no additional assistance from techniques such as pixel binning, meaning our preliminary results are conservative.

Table 7 reports SNR values for both mid-latitude summer and mid-latitude winter atmospheric models. We observe

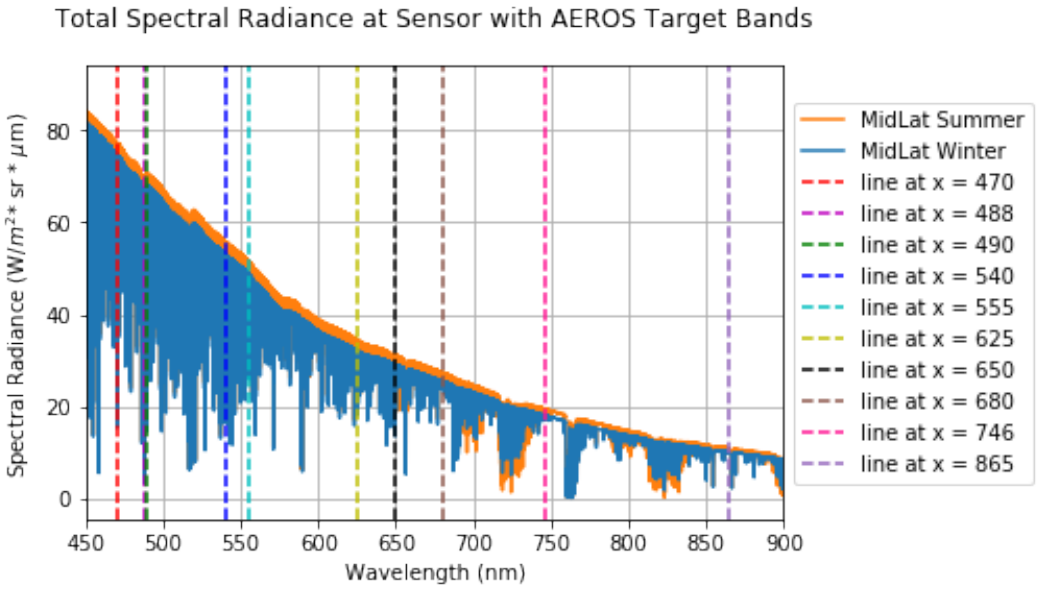


Fig. 13 TOA radiance from MODTRAN model output with target band centers overlaid for both MidLat Summer and MidLat Winter atmospheric Models

that while winter atmospheric conditions tend to reduce SNR compared with summer conditions, effects from seasonal variations on the overall measurement are minimal. In conclusion, our preliminary results show that we can achieve ocean color observations with comfortable signal margin given our current sensor configuration.

Table 7 Total radiance (W*m^{-2}*μm^{-1}*sr^{-1}) and corresponding SNR (dB) for each target band center where ΔSNR expresses seasonal variations between the two atmospheric models

Band Center (nm)	Total Rad Summer	Total Rad Winter	SNR Summer	SNR Winter	ΔSNR
470	72.8	70.7	17.24	17.17	0.07
488	64.1	62.0	17.04	16.95	0.09
490	61.8	61.7	16.95	16.95	0.00
540	51.9	49.4	16.77	16.65	0.12
555	48.7	46.1	16.69	16.55	0.14
625	33.1	30.9	16.05	15.89	0.16
650	29.0	27.9	15.82	15.73	0.09
680	27.1	25.2	15.77	15.60	0.17
746	19.3	17.9	15.16	14.98	0.18
865	10.5	9.7	13.97	13.76	0.21

VIII. Conclusion

The AEROS mission will demonstrate use of a custom, miniaturized multi-spectral imager to sense ocean color in coastal regions. We have assessed multiple orbit options for mission and orbital lifetime, power generation, and ROI coverage. We developed two MODTRAN models that predict at-sensor radiance specific to our region of interest, sensor configuration and orbit placement. Our radiometric tool estimates signal-to-noise ratios for each of the AEROS target bands, and preliminary results show that the planned sensor configuration is sufficient for measuring ocean radiance

Downloaded by MIT Libraries on October 26, 2026 | http://arc.aiaa.org | DOI: 10.2514/6.2021-4102

with at least 10 dB signal margin across all target bands. Lastly, we observe that seasonal variation has little effect on our target measurement, though additional work is required to assess effects from other sources of interference.

AEROS offers a low SWaP solution for space-based, multi-spectral ocean color measurements that both supplement and complement existing observations. A successful demonstration could improve ocean color measurements along the Portuguese coast, space-qualify the miniaturized multi-spectral imager, and provide useful data for regional climate and weather models. An AEROS constellation could serve to improve temporal resolution for ocean color observations, survey larger and more diverse regions of interest, and improve access to established environmental networks such as ARGOS.

A. Future Work

Now that we have developed our radiometry tool and understand the signal margin at each desired imaging band, next steps include assessing our anticipated loss in image interpretability relative to a shifting SNR. This loss is represented by a value on the National Imagery Interpretability Rating Scale (NIIRS) and is linearly related to the noise-equivalent change in reflection (NE$\Delta\rho$) [29]. Together, they compute the minimum viable signal that the imager must see, above all noise factors, to not lose image integrity [29]. Our team intends to explore the effects of more advanced pointing capabilities, as well as how varying atmospheric conditions such as clouds, rain and fog at lower altitudes impact the resulting SNR. Lastly, we intend to test our sensor in a lab with a controlled source in our final design configuration to determine its realistic behavior.

Given the novel configuration of our minituraized multi-spectral imager, the AEROS team is investigating integration of an additional, simple RGB camera to provide reference images for identical observation scenes. Additional investigation is underway to assess use of the multi-spectral imager to collect high-quality RGB images, though having redundant imagers is ideal if volume allows.

Acknowledgments

We acknowledge AGI, an Ansys company, for its Systems Tool Kit (STK) software, which was used for orbit analysis for the AEROS mission. The AEROS project is supported by MIT Portugal Partnership 2030 (MPP2030), and the work supports both the multinational "Atlantic Interactions" research efforts and UN sustainable development goals.

References

[1] Jonasdottir, S., "State of the Earth´s Oceans," 2016. URL http://www.sustain.dtu.dk/about/sustain-2016, sustain Abstract S-3; Sustain-ATV Conference 2016 : Creating Technology for a Sustainable Society ; Conference date: 30-11-2016 Through 30-11-2016.

[2] Drebes, M. H. M. E. G., *Marine Phytoplankton*, Schweizerbart Science Publishers, Stuttgart, Germany, 2009. URL http://www.schweizerbart.de//publications/detail/isbn/9783510613922/Kleine_Senckenberg_Reihe_Nr_49_Marine.

[3] "The Ocean Conference Factsheet: People and Oceans," technical pamphlet, 2017.

[4] Mouw, C. B., Hardman-Mountford, N. J., Alvain, S., Bracher, A., Brewin, R. J. W., Bricaud, A., Ciotti, A. M., Devred, E., Fujiwara, A., Hirata, T., Hirawake, T., Kostadinov, T. S., Roy, S., and Uitz, J., "A Consumer's Guide to Satellite Remote Sensing of Multiple Phytoplankton Groups in the Global Ocean," *Frontiers in Marine Science*, Vol. 4, 2017, p. 41. https://doi.org/10.3389/fmars.2017.00041, URL https://www.frontiersin.org/article/10.3389/fmars.2017.00041.

[5] McCandles, S., "The origin, evolution and legacy of SEASAT," *IGARSS 2003. 2003 IEEE International Geoscience and Remote Sensing Symposium. Proceedings (IEEE Cat. No.03CH37477)*, Vol. 1, 2003, pp. 32–34 vol.1. https://doi.org/10.1109/IGARSS.2003.1293669.

[6] Emery, W., and Camps, A., "Chapter 2 - Basic Electromagnetic Concepts and Applications to Optical Sensors," *Introduction to Satellite Remote Sensing*, edited by W. Emery and A. Camps, Elsevier, 2017, pp. 43–83. https://doi.org/10.1016/B978-0-12-809254-5.00002-6, URL https://www.sciencedirect.com/science/article/pii/B9780128092545000026.

[7] Emery, W., and Camps, A., "Chapter 3 - Optical Imaging Systems," *Introduction to Satellite Remote Sensing*, edited by W. Emery and A. Camps, Elsevier, 2017, pp. 85–130. https://doi.org/10.1016/B978-0-12-809254-5.00003-8, URL https://www.sciencedirect.com/science/article/pii/B9780128092545000038.

[8] Martin, S., "Background," *An Introduction to Ocean Remote Sensing*, Cambridge University Press, 2014, 2nd ed., pp. 1–34. https://doi.org/10.1017/CBO9781139094368.004.

Downloaded by MIT Libraries on October 26, 2026 | http://arc.aiaa.org | DOI: 10.2514/6.2021-4102

[9] Wenny, B. N., "Overview of NASA Earth Observing Systems Terra and Aqua moderate resolution imaging spectroradiometer instrument calibration algorithms and on-orbit performance," *Journal of Applied Remote Sensing*, Vol. 3, No. 1, 2009, p. 032501. https://doi.org/10.1117/1.3180864, URL http://remotesensing.spiedigitallibrary.org/article.aspx?doi=10.1117/1.3180864.

[10] "Terra & Aqua Moderate Resolution Imaging Spectroradiometer (MODIS) - LAADS DAAC," , 2021. URL https://ladsweb.modaps.eosdis.nasa.gov/missions-and-measurements/modis/.

[11] "Visible Infrared Imaging Radiometer Suite (VIIRS) - LAADS DAAC," , 2021. URL https://ladsweb.modaps.eosdis.nasa.gov/missions-and-measurements/viirs/.

[12] "Copernicus Sentinel-3 Ocean and Land Colour Instrument (OLCI) - LAADS DAAC," , 2021. URL https://ladsweb.modaps.eosdis.nasa.gov/missions-and-measurements/olci/.

[13] Vane, G., Green, R. O., Chrien, T. G., Enmark, H. T., Hansen, E. G., and Porter, W. M., "The airborne visible/infrared imaging spectrometer (AVIRIS)," *Remote Sensing of Environment*, Vol. 44, No. 2, 1993, pp. 127–143. https://doi.org/https://doi.org/10.1016/0034-4257(93)90012-M, URL https://www.sciencedirect.com/science/article/pii/003442579390012M, airbone Imaging Spectrometry.

[14] Cardoso, N. F. S., "Development of an ARGOS beacon for the VORSat CubeSat," , 2012.

[15] "Spin.Works Hyperspectral Camera," technical datasheet, Spin.Works, ????

[16] Nations, U., *The Second World Ocean Assessment*, Vol. I, Related Goals, 2021. URL https://sdgs.un.org/publications/launch-second-world-ocean-assessment-woa-ii-volume-i-32884.

[17] Baron, J., "Linescan Hyperspectral Image Sensor," company released, ????

[18] IADC Steering Group and Working Group 4, "IADC Space Debris Mitigation Guidelines Rev. 3," , 2021. URL https://www.iadc-home.org/documents_public/view/id/172#u.

[19] Wertz, J. R., Everett, D. F., and Puschell, J. J., *Space Mission Engineering: The New SMAD*, Space Technology Library, Microcosm Press, 2011.

[20] McCluney, W., *Introduction to Radiometry and Photometry, Second Edition*, Artech House applied photonics series, Artech House Publishers, 2014. URL https://books.google.com/books?id=w-jmBgAAQBAJ.

[21] Andor, "Radiometry and Photometry Explained," , ???? URL https://andor.oxinst.com/learning/view/article/radiometry-photometry.

[22] Schlyter, P., "Radiometry and photometry in astronomy," , ???? URL http://stjarnhimlen.se/comp/radfaq.html.

[23] Payne, C., "Auroral arc detection using a COTS spectral photometer for the Auroral Emission Radio Explorer (AERO) CubeSat Mission," phdthesis, 01 2020.

[24] Keith, D. J., Lunetta, R. S., and Schaeffer, B. A., "Optical Models for Remote Sensing of Colored Dissolved Organic Matter Absorption and Salinity in New England, Middle Atlantic and Gulf Coast Estuaries USA," *Remote Sensing*, Vol. 8, No. 4, 2016. URL https://www.mdpi.com/2072-4292/8/4/283.

[25] Kirk, J., "Light and Photosynthesis in Aquatic Systems," *Light and Photosynthesis in Aquatic Ecosystems, third edition*, Vol. Vol. VI, 2010, pp. 1–651. https://doi.org/10.1017/CBO9781139168212.

[26] Dutkiewicz, S., Hickman, A. E., Jahn, O., Henson, S., Beaulieu, C., and Monier, E., "Ocean colour signature of climate change," *Nature Communications*, Vol. 10, No. 1, 2019, p. 578.

[27] Sun, D., Su, X., Qiu, Z., Wang, S., Mao, Z., and He, Y., "Remote Sensing Estimation of Sea Surface Salinity from GOCI Measurements in the Southern Yellow Sea," *Remote Sensing*, Vol. 11, No. 7, 2019. URL https://www.mdpi.com/2072-4292/11/7/775.

[28] Jr., R. E. E., Turpie, K. R., Fireman, G. F., Meister, G., Stone, T. C., Patt, F. S., Franz, B. A., Bailey, S. W., Robinson, W. D., and McClain, C. R., "VIIRS on-orbit calibration for ocean color data processing," *Earth Observing Systems XVII*, Vol. 8510, edited by J. J. Butler, X. Xiong, and X. Gu, International Society for Optics and Photonics, SPIE, 2012, pp. 560 – 577. https://doi.org/10.1117/12.930483, URL https://doi.org/10.1117/12.930483.

[29] Fiete, R. D., and Tantalo, T. A., "Comparison of SNR image quality metrics for remote sensing systems," *Optical Engineering*, Vol. 40, No. 4, 2001, pp. 574 – 585. https://doi.org/10.1117/1.1355251, URL https://doi.org/10.1117/1.1355251.

Downloaded by MIT Libraries on October 26, 2026 | http://arc.aiaa.org | DOI: 10.2514/6.2021-4102

[30] Merken, P., and Vandersmissen, R., "DARK CURRENT AND INFLUENCE OF TARGET EMISSIVITY," white paper, Xenics Infrared Solutions, 2016. URL https://applied-infrared.com.au/images/pdf/Dark%20current%20and%20influence%20of%20target%20emissivity.pdf.

[31] Fry, P., Noble, P., and Rycroft, R., "Fixed-pattern noise in photomatrices," *IEEE Journal of Solid-State Circuits*, Vol. 5, No. 5, 1970, pp. 250–254. https://doi.org/10.1109/JSSC.1970.1050122.

[32] "Read noise in CMOS cameras: only rms is meaningful," online, ???? URL https://camera.hamamatsu.com/jp/en/technical_guides/read_noise/index.html.

[33] Berk, A., Anderson, G. P., Acharya, P. K., Bernstein, L. S., Muratov, L., Lee, J., Fox, M., Adler-Golden, S. M., Jr., J. H. C., Hoke, M. L., Lockwood, R. B., Gardner, J. A., Cooley, T. W., Borel, C. C., Lewis, P. E., and Shettle, E. P., "MODTRAN5: 2006 update," *Algorithms and Technologies for Multispectral, Hyperspectral, and Ultraspectral Imagery XII*, Vol. 6233, edited by S. S. Shen and P. E. Lewis, International Society for Optics and Photonics, SPIE, 2006, pp. 508 – 515. https://doi.org/10.1117/12.665077, URL https://doi.org/10.1117/12.665077.

[34] Berk, A., Conforti, P., and Hawes, F., "An accelerated line-by-line option for MODTRAN combining on-the-fly generation of line center absorption within 0.1 cm-1 bins and pre-computed line tails," *Algorithms and Technologies for Multispectral, Hyperspectral, and Ultraspectral Imagery XXI*, Vol. 9472, edited by M. Velez-Reyes and F. A. Kruse, International Society for Optics and Photonics, SPIE, 2015, pp. 405 – 415. https://doi.org/10.1117/12.2177444, URL https://doi.org/10.1117/12.2177444.

[35] Mobley, C., "Lambertian BRDFs," , 2021.

[36] Piazzola, J., van Eijk, A. M. J., and de Leeuw, G., "Extension of the Navy aerosol model to coastal areas," *Optical Engineering*, Vol. 39, No. 6, 2000, pp. 1620 – 1631. https://doi.org/10.1117/1.602538, URL https://doi.org/10.1117/1.602538.

[37] Ientilucci, E. J., "Using MODTRAN Predicting Sensor-Reaching Radiance," 2007. URL http://www.cis.rit.edu/~ejipci/Reports/Modtran_lab.pdf.

[38] Ientilucci, E., "Leveraging Lidar Data to Aid in Hyperspectral Image Target Detection in the Radiance Domain," 2012. https://doi.org/10.1117/12.919808.

[39] Pu, R., Gong, P., and Biging, G., "Simple calibration of AVIRIS data and LAI mapping of forest plantation in southern Argentina," *International Journal of Remote Sensing - INT J REMOTE SENS*, Vol. 24, 2003, pp. 4699–4714. https://doi.org/10.1080/0143116031000082433.

[40] McClain, C. R., and Meister, G., "Mission Requirements for Future Ocean-Colour Sensors," Tech. Rep. 13, IOCCG, 2012. URL https://ioccg.org/wp-content/uploads/2015/10/ioccg-report-13.pdf.

[41] "Photography — Electronic still-picture imaging — Noise measurements," Technical Standard 15739:2017, International Organization for Standardization (ISO), 2017.

Downloaded by MIT Libraries on October 26, 2026 | http://arc.aiaa.org | DOI: 10.2514/6.2021-4102